Japanese Journal of Applied Physics

The Japan Society of Applied Physics

PROGRESS REVIEW • OPEN ACCESS

Material design strategies for emulating neuromorphic functionalities with resistive switching memories

To cite this article: Panagiotis Bousoulas *et al* 2022 *Jpn. J. Appl. Phys.* **61** SM0806

View the article online for updates and enhancements.

You may also like

- Oxygen annealing effect on resistive switching characteristics of multilayer CeO_2/Al/CeO_2 resistive random-access memory
Muhammad Ismail, Sobia Ali Khan, Mehr Khalid Rahmani et al.

- Parasitic resistive switching uncovered from complementary resistive switching in single active-layer oxide memory device
Lisha Zhu, Wei Hu, Chao Gao et al.

- Modulation of nonlinear resistive switching behavior of a TaO_x-based resistive device through interface engineering
Zongwei Wang, Jian Kang, Zhizhen Yu et al.

This content was downloaded from IP address 164.11.25.126 on 04/06/2024 at 12:56

OPEN ACCESS

Japanese Journal of Applied Physics **61**, SM0806 (2022)

PROGRESS REVIEW

https://doi.org/10.35848/1347-4065/ac7774

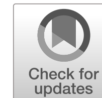

Material design strategies for emulating neuromorphic functionalities with resistive switching memories

Panagiotis Bousoulas[1*], Stavros Kitsios[1], Theodoros Panagiotis Chatzinikolaou[2], Iosif-Angelos Fyrigos[2], Vasileios Ntinas[2], Michail-Antisthenis Tsompanas[2], Georgios Ch. Sirakoulis[2], and Dimitris Tsoukalas[1]

[1]*School of Applied Mathematical and Physical Sciences, National Technical University of Athens, Iroon Polytechniou 9, 15772, Greece*
[2]*Department of Electrical and Computer Engineering, Democritus University of Thrace, Xanthi 67100, Greece*

[*]E-mail: panbous@mail.ntua.gr

Received February 18, 2022; revised April 19, 2022; accepted June 9, 2022; published online August 18, 2022

Nowadays, the huge power consumption and the inability of the conventional circuits to deal with real-time classification tasks have necessitated the devising of new electronic devices with inherent neuromorphic functionalities. Resistive switching memories arise as an ideal candidate due to their low footprint and small leakage current dissipation, while their intrinsic randomness is smoothly leveraged for implementing neuromorphic functionalities. In this review, valence change memories or conductive bridge memories for emulating neuromorphic characteristics are demonstrated. Moreover, the impact of the device structure and the incorporation of Pt nanoparticles is thoroughly investigated. Interestingly, our devices possess the ability to emulate various artificial synaptic functionalities, including paired-pulsed facilitation and paired-pulse depression, long-term plasticity and four different types of spike-dependent plasticity. Our approach provides valuable insights from a material design point of view towards the development of multifunctional synaptic elements that operate with low power consumption and exhibit biological-like behavior.
© 2022 The Author(s). Published on behalf of The Japan Society of Applied Physics by IOP Publishing Ltd

1. Introduction

The discipline of neuromorphic engineering has transformed the related information technologies by employing electronic devices capable of emulating the functions of the biological neural networks at a hardware level. The driving force behind this endeavor is the perspective of imitating the human brain that has the ability to deal—among others—with cognitive tasks under extremely low power consumption.[1,2] Currently, the conventional CMOS systems operate under the von Neumann principle, which imposes the data transfer between the processing and storage units.[3–5] However, this approach leads inevitably to the accumulation of an enormous amount of data that demand elevated power supply requirements. Furthermore, the relatively big size of the CMOS transistors limits significantly their integration density. It is interesting to notice that as far as the implementation of an artificial synapse is concerned, a relatively large circuit from a least ten transistors is required whereas even more transistors are integrated towards the realization of an artificial neuron.[6,7] It is thus obvious that the current approaches are not compatible with the practical operation of large neural networks. Under this direction, the appearance of resistive switching devices with rich internal dynamic processes paves the way towards the implementation of novel hardware-based neural networks with low leakage power dissipation, as well as by exploiting the threshold switching effect of the devices, spiking oscillators with bio-inspired computing capabilities have been verified.[8–12] Moreover, taking into account the tremendous density of the human brain's neural networks (about 10^{12} spiking neurons are interconnected by 10^{15} synaptic junctions), the simple metal–insulator–metal (MIM) structure of resistive random access memory (RRAM) offers great integration perspectives (especially under the light of 3D crossbar configuration[13]).

In addition, the integration of novel material configurations (such as nanoparticles (NPs) or 2D materials) that possess superior physical properties could also provide an additional degree of freedom towards tuning the device reliability issues and implementation of quite complex neuromorphic computing functionalities.[14,15] Although there are several reports in the literature regarding the utilization of the resistive switching effect towards the implementation of artificial synaptic and neuron characteristics[16–18] several challenges should be addressed before memristive neuromorphic hardware goes mainstream.[19] These include the device reliability, the degree of analogue/digital transitions, the programming variability and energy per spike consumption. More specifically:

(a) Materials' inherent stochasticity and lack of predictability generate high write noise. As a result, it is practically impossible to attain a large tunable conductance range, while the local chemical and thermal instabilities of the material are also a critical issue.
(b) Implementation of synaptic property characteristics and spiking neuron activity within the same memory element is not trivial, since the design requirements of the artificial synapses are quite different with respect to artificial neurons. The role of the synapse is to control the flow of information by weight modulation whereas the neuron assembles the information and releases it (fire activity) if a threshold value is met. Until now, there are reports regarding the employment of discrete resistive neuron and synapse electronic elements in order to build a fully memristive neural network, which increases dramatically the design complexity between these two platforms.[20,21]
(c) Furthermore, the main challenge related to the performance of an artificial neuromorphic device is the achievement of ultra-low-power operation, similar to that recorded within the brain. More specifically, the energy consumption by the artificial neuron should be as low as 10 fJ within a complete firing activity cycle.[22]

Content from this work may be used under the terms of the Creative Commons Attribution 4.0 license. Any further distribution of this work must maintain attribution to the author(s) and the title of the work, journal citation and DOI.

© 2022 The Author(s). Published on behalf of The Japan Society of Applied Physics by IOP Publishing Ltd

For the synapses, power consumption at the range of 1–100 fJ is required in order to be compatible with the total power consumption of the human brain.[23] This implies that the energy losses from the leakage currents within the crossbar array should be very small and a strong nonlinear (threshold type) performance should be achieved.

To address these technological challenges, it is apparent that a physics-driven device engineering and materials architecture is required in order to divulge the necessary trade-offs between the above-mentioned stringent device requirements, as well as to enhance the various neuron and synaptic device characteristics.

The goal of this review is to provide a comprehensive outline of valence change memories (VCM) and conductive bridge memories (CBRAM)-based device architectures and at the same time highlight the influence of the Pt NPs on the total memristive and neuromorphic behavior. Our work paves the way for the development of novel artificial synaptic elements with low power consumption and high integration density for the potential implementation of fully memristive neural networks for various applications. Interestingly, the utilization of bilayer or trilayer configurations by tuning during the fabrication of the oxygen content of each layer is a quite simple technique to reduce the operating current values We have to underline, that as far as VCM structures are concerned, the total thickness of the bilayer (Fig. 1) and trilayer (Fig. 4) was 45 and 70 nm, respectively. For the CBRAM-based devices, the total thickness was 20 nm in all cases. Moreover, all the fabricated devices exhibited a capacitor-like structure with square electrodes of 100 μm lateral dimension.

2. Resistive switching memories and neuromorphic properties

RRAMs are either volatile or non-volatile memory devices with a typical MIM structure that has a quite small footprint.[24] Several studies have revealed that the resistive switching effect involves a series of thermal and electric field accelerated redox reactions.[25] Depending on the underlying nature of the species involved in the atomic configuration, the devices can be classified as either VCM—RAMs or CBRAMs. In the former case, the conductance tuning is originated from the migration of oxygen vacancies whereas in the latter the migration of electrochemically active metallic ions (e.g. Ag, Cu) generates a metallic chain that connects the two electrodes.[26] We have to underline that the rich nature of the switching effect within the CBRAM configuration permits the manifestation of various switching modes, such as threshold and bipolar switching, which can be utilized for various applications.[27] However, the intrinsic stochasticity of the switching effect, that has been extensively investigated in Ref. 28, can jeopardize the ability to emulate all these properties in one single memory cell.[29] Although there are some reports in the literature regarding the implementation of both neuron and synaptic activity by a single electronic device, they incorporate either three-terminal architecture[30] (that it is not efficient in terms of ultra-packed integration) or relatively high operating biases[31] (that are not compatible in terms of power consumption).

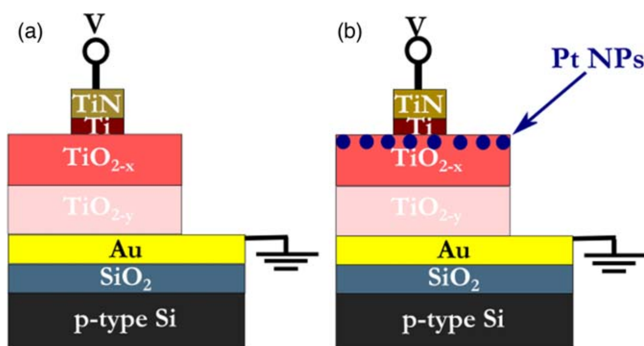

Fig. 1. (Color online) Schematic illustration of the cross-section of the (a) reference and the (b) Pt NPs-based memory devices.

Within the brain structure, neurons encrypt information packages by releasing small voltage pulses that are called action potentials or spiking neuronal signals. These signals are subsequently propagated through the colossal parallel processing network of the human brain to millions of other neurons. Along with the distribution of neurons in the brain, the vast grid of synapses consists of a biological neural network that is responsible for human emotion, perception, forgetting, learning and memory tasks.[32] While neurons operate towards the generation and propagation of action potential, the synapses are responsible for the processing and storage procedures. It is thus obvious that the synapses rule the brain architecture and configure its structural plasticity and colossal parallelism for the assigned tasks. Within the brain there are two types of synapses: (a) electrical synapses and (b) chemical synapses.[33] The pure electrical synapses characterize the direct contact between the pre- and post-synaptic neurons and function with a relatively big frequency. However, they do not exhibit any flexibility and signal modulation characteristics. For that reason, they are commonly detected at the early fetus stages, where no large-scale functional neural networks still exist. The most regular type of synapses is the chemical synapses that possess a small gap (~20–50 nm) between the pre- and post-synaptic layers. Accordingly, the synaptic efficiency or the junction strength can be adjusted according to the activities of the neurons. We have to underline that this quite important principle lies behind all the biological procedures that evolve within the human brain. Therefore, it is not surprising that a variety of synaptic plasticity properties have been found over the decades of intensive research in the neuroscience discipline.

The impressive characteristic of all the reported properties is that they cover a time constant between a few microseconds to several years. In this light, we can argue that the synaptic properties are generally divided into two major categories: short-term plasticity (STP) and long-term plasticity (LTP).[34] The STP is associated with quick response and information filtering whereas LTP is connected with the memory capacity and the dynamic modifications in synaptic strength. As concerns the STP properties, several types of plasticity effects that evolve within the range of microseconds to several minutes have been discovered, including analog conductance modulation (potentiation/depression), paired-pulse facilitation (PPF), paired-pulse depression (PPD) and augmentation. In contrast with short term memory (STM), long term memory (LTM) includes the long-term potentiation (LTPot), long-term depression effects, as well as

© 2022 The Author(s). Published on behalf of The Japan Society of Applied Physics by IOP Publishing Ltd

the transition from STP to LTP. The synaptic efficacy under LTP mode has a typical duration from several hours to years. Moreover, the distribution and firing activity of the incoming signals to the synapses from the neurons network, as well as the local dynamic synaptic weight modulation, resulting in the realization of some high-order synaptic plasticity characteristics with both long-term and short-term dynamics. These include the spike-time-dependent plasticity (STDP), the spike-rate-dependent plasticity,[35] the metaplasticity[36] and the hetero-synaptic plasticity effects.[37] Although the above-mentioned list of synaptic properties seems daunting and it is almost impossible to devise an electronic element capable of performing all these tasks, memristors arise as an ideal candidate in that direction. Despite their relatively simple MIM structure, resistive switching devices possess extremely rich and complicated internal mechanisms capable of emulating a variety of bio-realistic synaptic properties.[38] The critical issue is, however, to find a way in order to attain all these properties in one memristive device on-demand and in a reproducible and reliable manner.

3. Analog conductance tuning with bilayer and Trilayer-based VCM elements

The majority of the artificial neural networks (ANNs) operate under the backpropagation scheme,[39] which is strongly dependent on the linearity of the various conductance states to alleviate the relative synaptic weight update processes, as well as the peripheral circuit design.[40] Along these lines, TiO_{2-x}-based bilayer devices were fabricated by employing a room-temperature technique,[41,42] while the impact of the embedded Pt NPs was also explored.[43–45] A schematic illustration of the fabricated devices is presented in Fig. 1, while a thin film of pure Ti (4 nm) was used as an oxygen scavenging layer to enhance the stability of the switching effect.[46–49]

The recorded hysteresis curved are depicted in Fig. 2(a), where some distinct differences can be observed between the two samples. Interestingly, no electroforming procedure is required prior to device operation, which is regarded as of great importance for the peripheral circuit design. Additionally, the embedded Pt NPs facilitate the oxygen vacancy generation and thus enhanced switching ratios are recorded.[50] The switching effect is interpreted in terms of the formation of percolating CFs, whereas their existence is attributed to concrete results from atomic force microscopy images,[51,52] as well as the independence of the LRS from the total device area.[53] Besides, an intermediate surface density of Pt NPs of about 1×10^{12} NPs cm^{-2} was used with an average diameter of 3 nm [Fig. 2(b)]. It is also interesting to notice that the existence of NPs improves remarkably the statistical dispersion of the switching characteristics since impose the formation/annihilation of the conducting filament (CF) into specific locations.[54,55] Furthermore, the gradual modulation of the memristive effect is leveraged to precisely tune various conductance states and induce the respective potentiation/depression procedures. As can be ascertained from Fig. 3, although the Reference sample reveals a good degree of linearity during the potentiation process, the response of the depression procedure and the total cycling performance are not good.

As far as the Pt NPs embedded sample is concerned, smaller external signals are required to observe the continuous synaptic weight modulation pattern and the acquired responses are more stable. Nevertheless, the extracted conductance values quickly saturate after the application of about 3–5 pulses, due to the steeper switching transition of the Pt NPs sample, resulting in a poorer degree of linearity. As a result, there is a trade-off between the low-power consumption and the linearity factor. This effect is nicely captured when a trilayer configuration is employed for the implementation of artificial synaptic properties.[56,57] As can be observed from Fig. 4, the operating current values are just beyond 10 nA during the SET process, which greatly improves the power consumption of such types of devices. In addition, the switching transitions during both the SET/RESET cycles are quite smooth, which yields a quite linear pattern during the enforcement of the synaptic weight modulation measurements (Fig. 5). The device-to-device variability was also studied by examining the synaptic responses from 20 different memory elements [Fig. 5(b)]. However, relatively large pulses are acquired to implement the continuous conductance modulation pattern that could lead to an excess burden, in terms of incorporating the necessary peripheral circuits capable of delivering such big pulses.

4. Impact of the switching mode of CBRAM on the synaptic weight modulation properties

By considering that the VCM devices operate under the application of relatively big signals, CBRAM-based memory

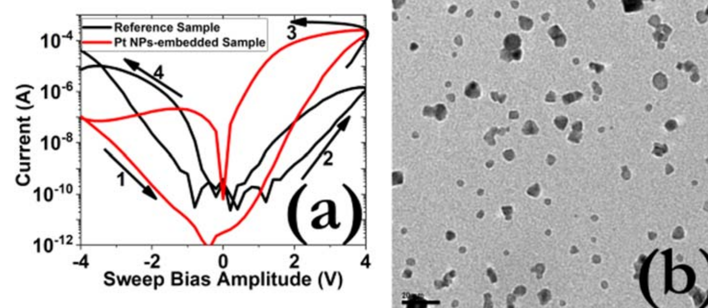

Fig. 2. (Color online) (a) I–V hysteresis curves of the two bilayer configurations under the application of 4V cycling bias. No compliance current (I_{cc}) limit was enforced during the implementation of the bipolar switching effect. The arrows in the graphs signify the switching direction while the sweep rate was 10 mV s^{-1}. Similar switching patterns were captured by starting the sweeps from 0V to $|V_{max}|$ (not shown here). The underlying idea to start sweeps from negative voltage is to automate the consecutive cycling measurement procedure. (b) TEM plan view image of the Pt NPs. The scale bar corresponds to 20 nm.[53]

© 2022 The Author(s). Published on behalf of The Japan Society of Applied Physics by IOP Publishing Ltd

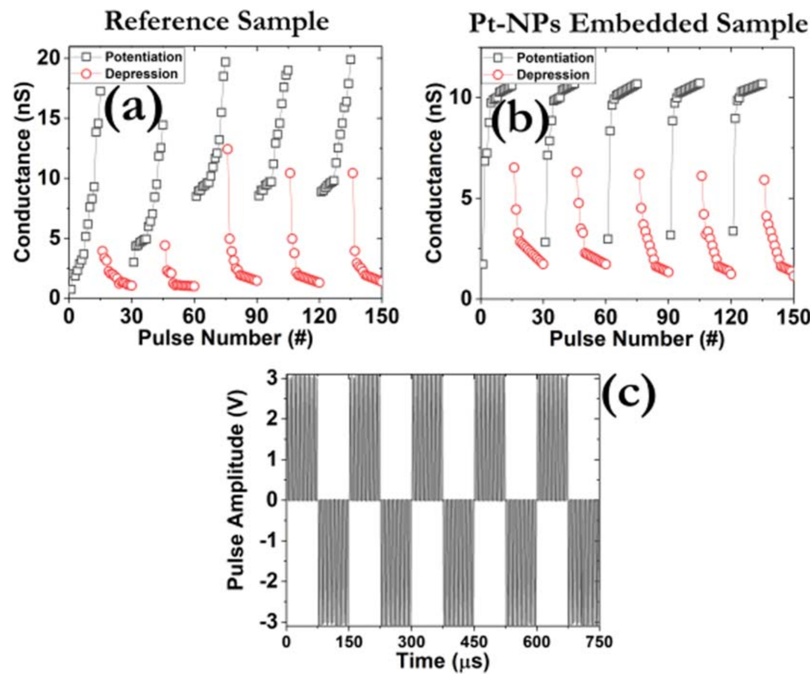

Fig. 3. (Color online) Synaptic potentiation and depression responses by enforcing identical pulse sequences. For the Reference sample ±5 V, 1 μs were applied whereas for Pt NPs embedded sample square pulses with lower amplitude were employed (±3 V, 1 μs). The conductance values were extracted at a read-out voltage of 0.5 V after each pulse.[53] (c) Depiction of the applied pulse sequence for the Pt NPs sample. A similar protocol was enforced for the reference sample by applying square pulses with higher amplitude. The rise and delay time of the pulse sequence was 1 μs.

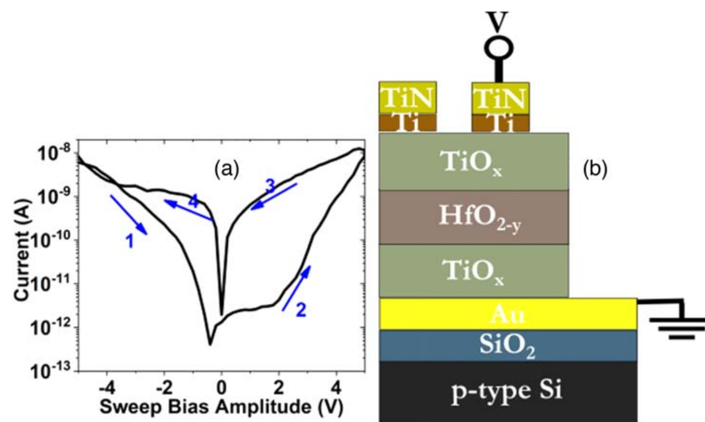

Fig. 4. (Color online) (a) I–V hysteresis pattern under the application of 5 V cycling bias. No I_{cc} is applied during the manifestation of the memristive effect. (b) Schematic illustration of the cross-section of the trilayer configuration.

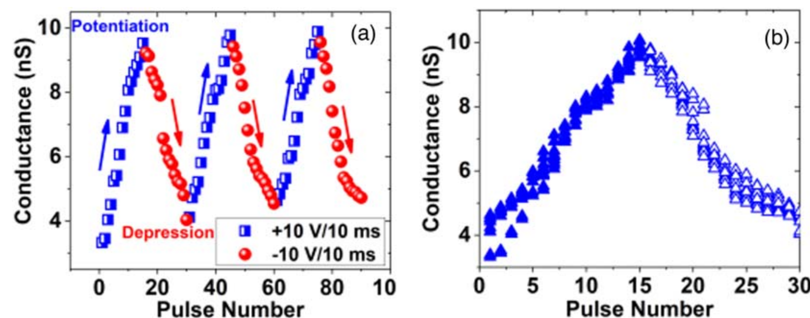

Fig. 5. (Color online) (a) Continuous conductance modulation during the implementation of the synaptic potentiation and depression procedures. (b) Cycling variability of the synaptic weight modulation.[56]

cells were explored to investigate their properties in emulating artificial synaptic characteristics. Figure 6 depicts the acquired I–V responses and the structure of the employed memory element. It is interesting to notice that the devices operate under the application of small DC signals (∼250–500 mV), whereas two different switching modes are captured. More specifically, a threshold or volatile switching mode and a bipolar of non-volatile switching mode are

© 2022 The Author(s). Published on behalf of The Japan Society of Applied Physics by IOP Publishing Ltd

recorded. For the threshold switching mode, no negative polarity bias is required to reduce the total resistance of the memristive element since the operating current is abruptly reduced before the 0 V. In striking contrast, for the bipolar switching mode, a negative polarity bias is enforced to induce the RESET transition and switch the device to the LRS state. Although in the literature there are reports concerning the interpretation of this effect,[58,59] they cannot deal with the ultra-small relaxation times (<1 μs) of the proposed devices. For that reason, a comprehensive numerical model was developed to interpret the coexistence of threshold and bipolar switching by considering the size-dependent melting process of the Ag nanoclusters (NCs),[60] which are formed due to material precipitation from the enhanced solid-solubility of Ag,[61] due to their thermal-out diffusion. In particular, three partial differential equations were simultaneously and self-consistently solved to simulate the whole memristive pattern and calculate the effective diameter of the CF. The effective diameter is a single compact value. The term effective is introduced since the bottom diameter of the CF (ϕ_B) exhibits a different distribution of the respective diameter at the top electrode/dielectric interface (ϕ_A). On top of that, bilayer-based CBRAM devices were fabricated to investigate material-based strategies to tune the manifestation of the two switching modes.[62] The acquired results are depicted in Fig. 7, whereas the impact of the active electrode on the switching performance has been also extensively studied.[63] The SiO_2-based bilayer configuration was used to reduce the operating current values. More specifically, as can be observed from Figs. 6(a) and 7(a), the current values for the ON-state have been reduced by about two orders of magnitude. Moreover, for the bilayer structure, only one switching mode is recorded (i.e. bipolar switching), in striking contrast with the single-layer SiO_2 CBRAM where two switching modes (i.e. threshold and bipolar) co-exist in the same device. This effect is quite important since significant opportunities arise for the emulation of the synaptic depression characteristics without reversing the polarity of the applied signal. It is interesting to notice that the coexistence between threshold switching and bipolar memristive cycling permits the implementation of the synaptic depression process by just tuning the frequency of the pre-synaptic signal [Fig. 8(a)], whereas no such effect is attainable when the devices operate only with the bipolar switching mode. Moreover, as can be ascertained from Fig. 8(a), the application of a low/high frequency leads to a decrease/increase of the current responses for the single-layer structure, whereas no such effect is recorded for the bilayer configuration [Fig. 8(b)]. The origins of this effect are closely connected with the CF growth mechanism. Under the threshold switching mode, the formed CF is quite unstable and the enforcement of external signals with relatively small frequency cannot sustain a permanent conductive path between the two operating electrodes. This phenomenon is also of great importance since alleviates the design of the respective circuit that supplies with the train of pulses the memory cell, since pulse with the same polarity has to be delivered.

5. Enhanced conductance linearity with bilayer CBRAM

The impact of Pt NPs,[64] as well as the incorporation of a hetero-bilayer configuration was also examined to investigate the linearity of the conductance update procedure.[65] The extracted hysteresis spectra are depicted in Fig. 9, where it can be ascertained the quite different responses of the fabricated samples. As far as the Pt NPs sample is concerned, the switching transitions are quite steep and only the threshold switching mode is recorded, regardless of the amplitude of the applied signal or the enforced I_{cc}. The underlying reason for this effect is the limited thermal conductivity value of the Pt NPs. Actually, the thermal conductivity value of Pt NPs is significantly smaller than the respective value of TiN.[66] Consequently, the generated heat during the device operation cannot efficiently be removed, and the formed CF can easily rupture. What's more, in case of a large increase of temperature within the device's active core, the thermal boundary conductance should also play a role in the whole memristive pattern. In addition, the interface roughness could affect the operation of CBRAM. More specifically, the high surface roughness of Pt NPs (∼5 nm) could lead to the formation of sharp tips that can significantly enhance the local electric field distribution.[65,67] On the other hand, a different effect takes place for the VO_x-based sample. Due to the bigger diffusivity value for Ag ion migration within this layer,[68] the operating current values are reduced below 1 μA. Moreover, only the bipolar switching mode is recorded for this specific device configuration, whereas the switching transitions are quite smooth, in striking contrast with the Pt NPs sample. This outcome has a unique influence on the implementation of a quite linear synaptic update pattern, as can be observed from Fig. 10. In more detail, the conductance adjustment procedures take place in a complete way between the two samples.

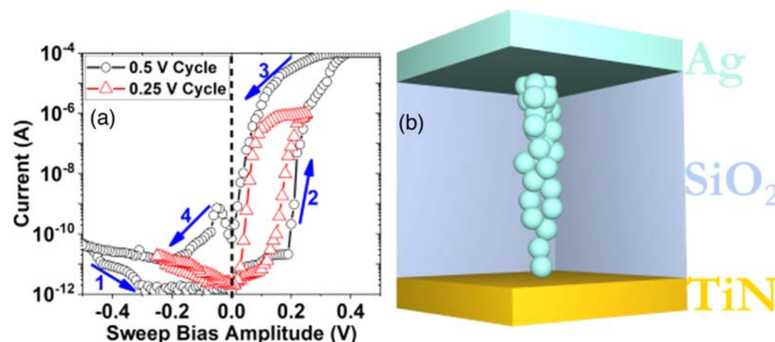

Fig. 6. (Color online) (a) I–V hysteresis pattern under the application of 0.25 and 0.5 V cycling bias. A constant I_{cc} of 100 μA was enforced during the manifestation of the bipolar switching effect. (b) Schematic illustration of the SiO_2-based structure.[60]

© 2022 The Author(s). Published on behalf of The Japan Society of Applied Physics by IOP Publishing Ltd

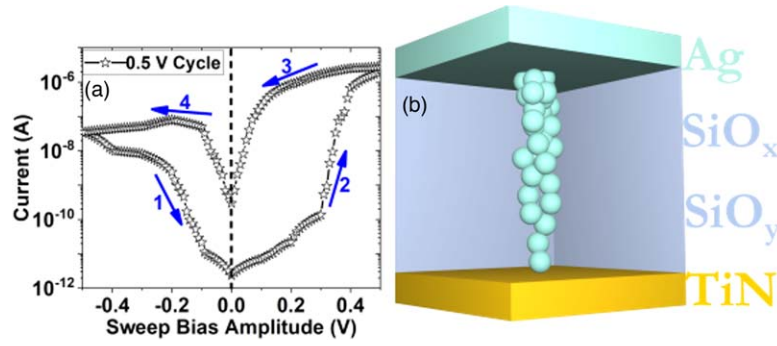

Fig. 7. (Color online) (a) *I–V* hysteresis pattern under the application of 0.5 V cycling bias. No I_{cc} was enforced during the manifestation of the bipolar switching effect. (b) Schematic illustration of the SiO_2-based bilayer structure.[62]

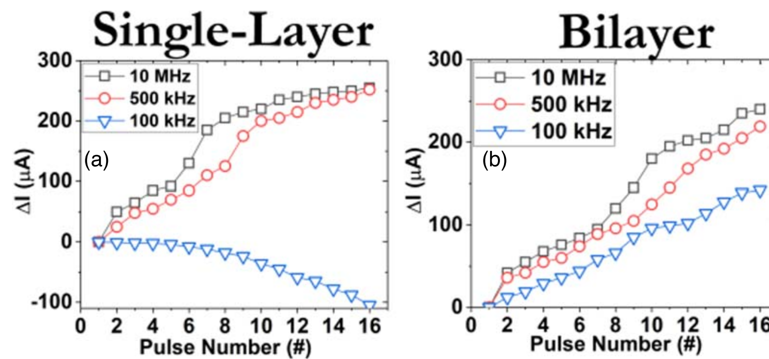

Fig. 8. (Color online) Synaptic weight modulation properties of (a) the single-layer and (b) the bilayer-based CBRAM configurations.[62] The data have been extracted after the application of square pulses with 0.3 V amplitude and 100 ns width.

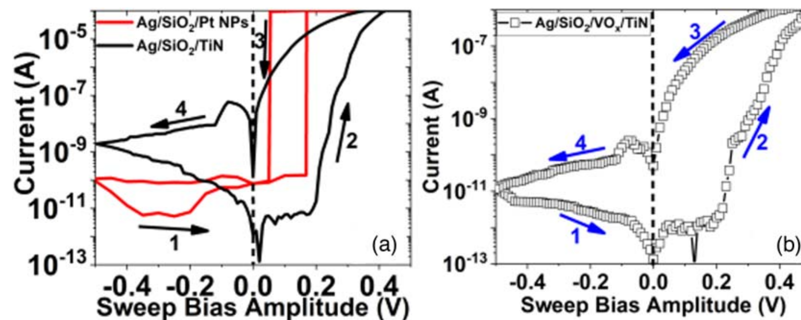

Fig. 9. (Color online) *I–V* hysteresis pattern of (a) the Pt NPs-based CBRAM, as well as the respective reference sample,[65] and (b) the bilayer configuration. A constant I_{cc} of 100 μA was enforced in all cases. The small variations between (a) and Fig. 6(a) are attributed to the device-to-device variability since the same sample was used in both cases.

As far as the Pt NPs sample is concerned, the recorded conductance values grow/fall after the enforcement of only 5 positive/negative pulses, whereas then a saturation effect is captured. As a result, a relatively high value for both α_ρ and α_d nonlinearity coefficients is measured. On the other hand, for the VO_x-based configuration, a different pattern is extracted. No saturation effect is recorded after the application of 15 positive and 15 negative square pulses, whereas the induced conductance values seem to follow a quite linear pattern. Therefore, the employment of the suitable material configuration is of great importance for the emulation of biological properties on demand.

6. Emulating various synaptic functionalities with Pt NPs-based CBRAM

The influence of the dense layer of Pt NPs, which was used as a bottom electrode, was examined for mimicking a wide range of artificial synaptic functionalities.[67,69] By taking into

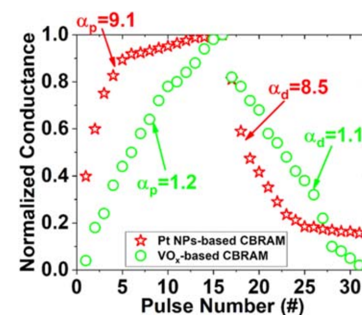

Fig. 10. (Color online) Continuous conductance modulation during the implementation of the synaptic potentiation and depression procedures for the Pt NPs-based device and the bilayer configuration.[65] The α_ρ and α_d coefficients stand for the degree of nonlinearity during the update of the conductance for the potentiation and depression procedures, respectively. The data have been collected after the application of 32 square pulses with ±V amplitude and 100 ns width (read-out voltage 100 mV/100 ns).

© 2022 The Author(s). Published on behalf of The Japan Society of Applied Physics by IOP Publishing Ltd

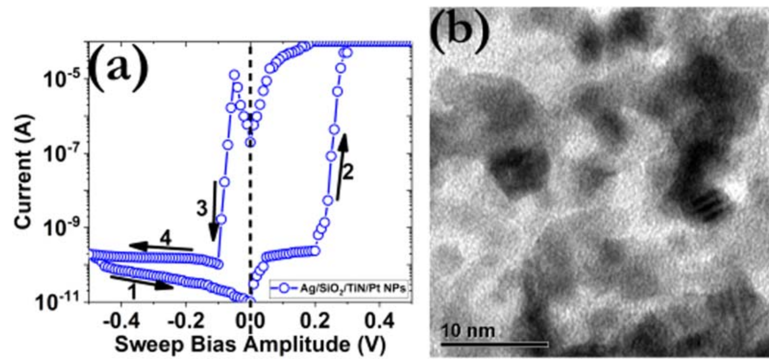

Fig. 11. (Color online) (a) Measured *I–V* characteristics under the application of $I_{cc} = 100\ \mu$A, respectively, for the Ag-based CBRAM. The sweep rate was 10 mV s^{-1}. (b) TEM plan view image of the dense layer of the Pt NPs. The scale bar corresponds to 10 nm.[69]

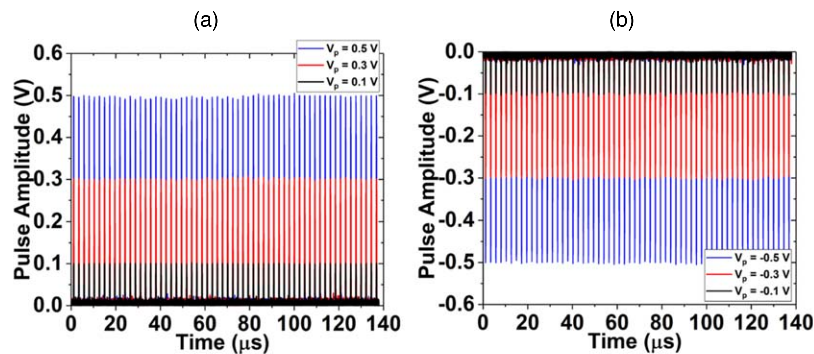

Fig. 12. (Color online) Evolution with the time of the pre-synaptic pulse profiles during the employment of the (a) potentiation and (b) depression procedures, under the application of a total of 60 pulses with 100 ns width and amplitudes of ±0.1 V, ±0.3 V and ±0.5 V, respectively.[69]

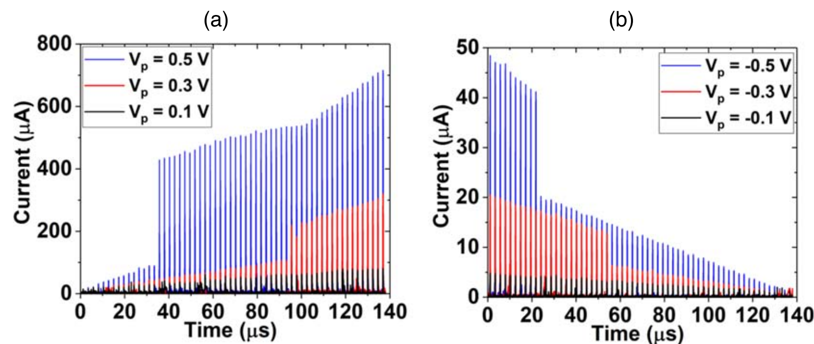

Fig. 13. (Color online) Evolution with the time of the post-synaptic current responses during the application of the (a) potentiation and (b) depression procedures, under the application of a total of 60 pre-synaptic pulses with 100 ns width and amplitudes of ±0.1 V, ±0.3 V and ±0.5 V, respectively.[69]

account that the manifestation of various neuromorphic properties is directly correlated with the growth mechanism of the percolating CFs, a reconfigurable synaptic pattern can be achieved by adjusting the effective diameter of the CF. Along these lines, the presence of NPs can impact the thermal accelerated migration of the ionic species, due to the local Joule heating distribution. Besides, a thin layer of 15 nm of TiN was used directly above the Pt NPs to induce the bipolar switching mode, which is required for the storage of the imposed synaptic weights. Figure 11(a) depicts the acquired hysteresis curve, where a huge switching ratio is obtained (∼106), while the SET/RESET transitions take place at about ∼220/−50 mV. Additionally, the TEM plan view image of the deposited NPs is presented in Fig. 11(b), where it can be observed that the deposited NPs do not follow any preferred morphology. An intermediate switching slope of ∼30 mV dec^{-1} (*A*) was recorded, which is beneficial for the implementation of the various synaptic functionalities. With the "intermediate switching slope" expression we imply that the transition slope is not as steep as in the case where a dense layer of Pt NPs is present [<1 mV dec^{-1} (*A*)] and not as smooth as in the case of the reference sample composed of Ag/SiO_2/TiN [∼80 mV dec^{-1} (*A*)]. The switching slope has been calculated from the inverse transition of the SET transition (the respective direction is indicated by arrow number 2).

Figures 12 and 13 display the pre and post-synaptic responses of the memristive element, respectively, which clearly illustrate the successful emulation of the PPF and PPD characteristics. According to this biological principle, during the application of two identical pre-synaptic signals, the second post-synaptic response becomes either bigger (PPF)

© 2022 The Author(s). Published on behalf of The Japan Society of Applied Physics by IOP Publishing Ltd

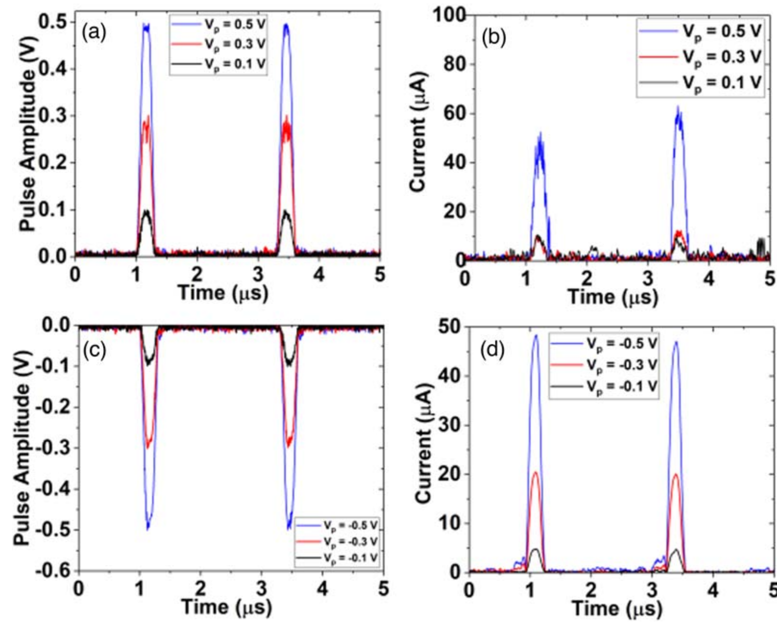

Fig. 14. (Color online) (a) Depiction of two consecutive input pulses (with various amplitudes) of (a) positive or (c) negative height and the corresponding current response of the SiO_2-based device, where the appropriate implementation of the paired-pulse (b) facilitation and (d) depression mechanism is demonstrated.

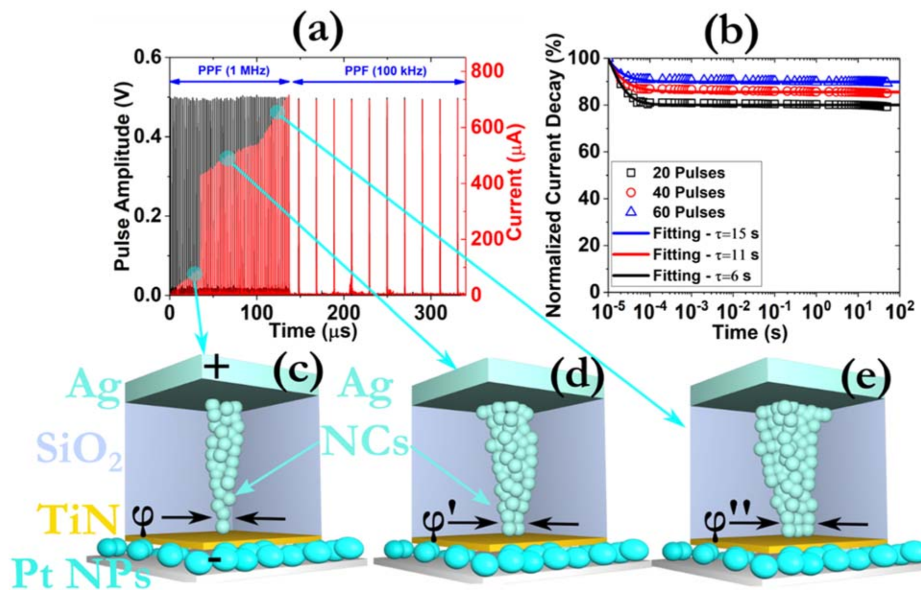

Fig. 15. (Color online) (a) Demonstration of the PPF effect by observing the post-synaptic current response after the application of a train of 70 pulses with the same width (100 ns), amplitude (0.5 V) and different frequency, (b) evolution with the time of the normalized current decay as a function of time demonstrating LTP synaptic behavior. The data have been collected after enforcing a train of 95 pulses with frequency 100 kHz after the application of 60 pulses with frequency 1 MHz, (c), (d), (e) schematic representation of the CF growth procedure during the application of the consecutive pulsing scheme. The symbol ϕ represents the effective diameter of the CF.[69]

or smaller (PPD), with respect to the first signal. It is also interesting to notice that we have the ability to reproduce such types of effects under the enforcement of signals as small as 100 mV. Earlier it was shown (Fig. 8) that one can achieve synaptic depression via positive pulse sequences at appropriate frequencies through structures in which threshold switching coexists with bipolar memristive cycling. Here is demonstrated that by reducing the amplitude of the applied signal the same effect can be also attained. It is also interesting to notice that the proposed devices possess the ability to reproduce such types of effects under the enforcement of signals as small as 100 mV. Interestingly, the application of a pre-synaptic signal with high amplitude leads to an abrupt increase in the post-synaptic response in a shorter period of time. More specifically, after the enforcement of 16 square pulses with +500 mV amplitude, the recorded current response is increased, whereas a comparable pattern is captured under the application of pulses with negative polarity. An inset has been also provided to highlight the corresponding current response of the device stack to more clearly the appropriate implementation of the PPF (depression) mechanism [Fig. 14].

On top of that, the STP and LTP effects were also attained from our devices by just tuning the frequency of the applied

© 2022 The Author(s). Published on behalf of The Japan Society of Applied Physics by IOP Publishing Ltd

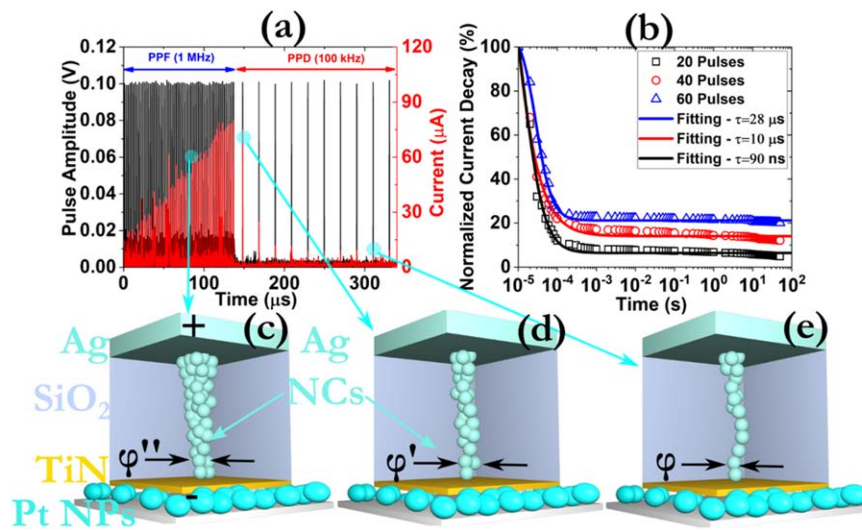

Fig. 16. (Color online) (a) Demonstration of the PPF to PPD transition effect by examining the post-synaptic current response after the enforcement of a train of 70 pulses with the same width (100 ns), amplitude (0.5 V) and different frequency, (b) evolution with the time of the normalized current decay as a function of time demonstrating STP synaptic behavior. The data have been collected after implementing a set of 95 pulses with frequency 100 kHz after the enforcement of 60 pulses with frequency 1 MHz, (c)–(e) schematic illustration of the CF growth procedure during the application of the consecutive pulsing scheme. The symbol ϕ denotes the effective diameter of the CF.[69]

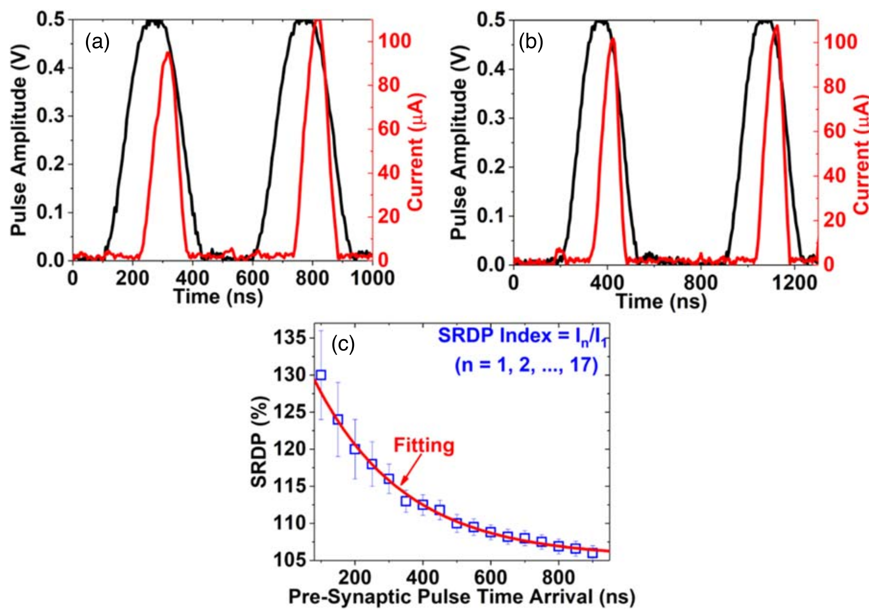

Fig. 17. (Color online) Experimental verification of the PPF effect as a function of the time interval between the pre-synaptic pulses. 17 different pulse intervals were investigated by enforcing two successive pulses of 0.5 V/100 ns while (a) and (b) reveal the post-synaptic responses for a delay time of 100 and 200 ns, respectively. (c) Distribution of the SRDP index (I_n/I_1) calculated by two consecutive pulses with time interval $100 \leqslant \Delta t \leqslant 900$ ns (I_1: 1st post-synaptic current, I_n: nth post-synaptic current, $n = 1, 2, 3, ..., 17$).[69]

pre-synaptic signal. The STM is related to the sensory part of the human memory, whereas the LTM describes the long-term memories of the human brain, according to the well-established model of Atkinson and Shiffrin.[70] As it is presented in Figs. 15 and 16, the acquired outcomes are attributed to the modulation of the effective CF's diameter, which influences the total current of the device. Along these lines, to deeply investigate the ability of the proposed devices to emulate the transition from the STP to LTP mode, a train of square pulses with different amplitude and frequency was applied. As can be observed from Fig. 16(a), under the application of pre-synaptic signals with +500 mV amplitude, the final current response that is recorded after the 70th pulse is maintained even when the applied frequency has been reduced from 1 MHz to 100 kHz since a robust CF has been formed, which cannot be ruptured easily [Figs. 16(c)–16(e)]. The decay rate of the post-synaptic current has been also monitored by enforcing a different number of square pulses, as can be seen from Fig. 16(b), where relatively big relaxation times (τ) were recorded that signify the successful implementation of the LTP effect. On the other hand, under the application of smaller pre-synaptic pules, in terms of amplitude, in combination with the previously reported frequency modulation process, the STM mode is captured [Fig. 17(a)] since quite short relaxation times (τ) have been measured [Fig. 17(b)]. This effect could be ascribed to the

© 2022 The Author(s). Published on behalf of The Japan Society of Applied Physics by IOP Publishing Ltd

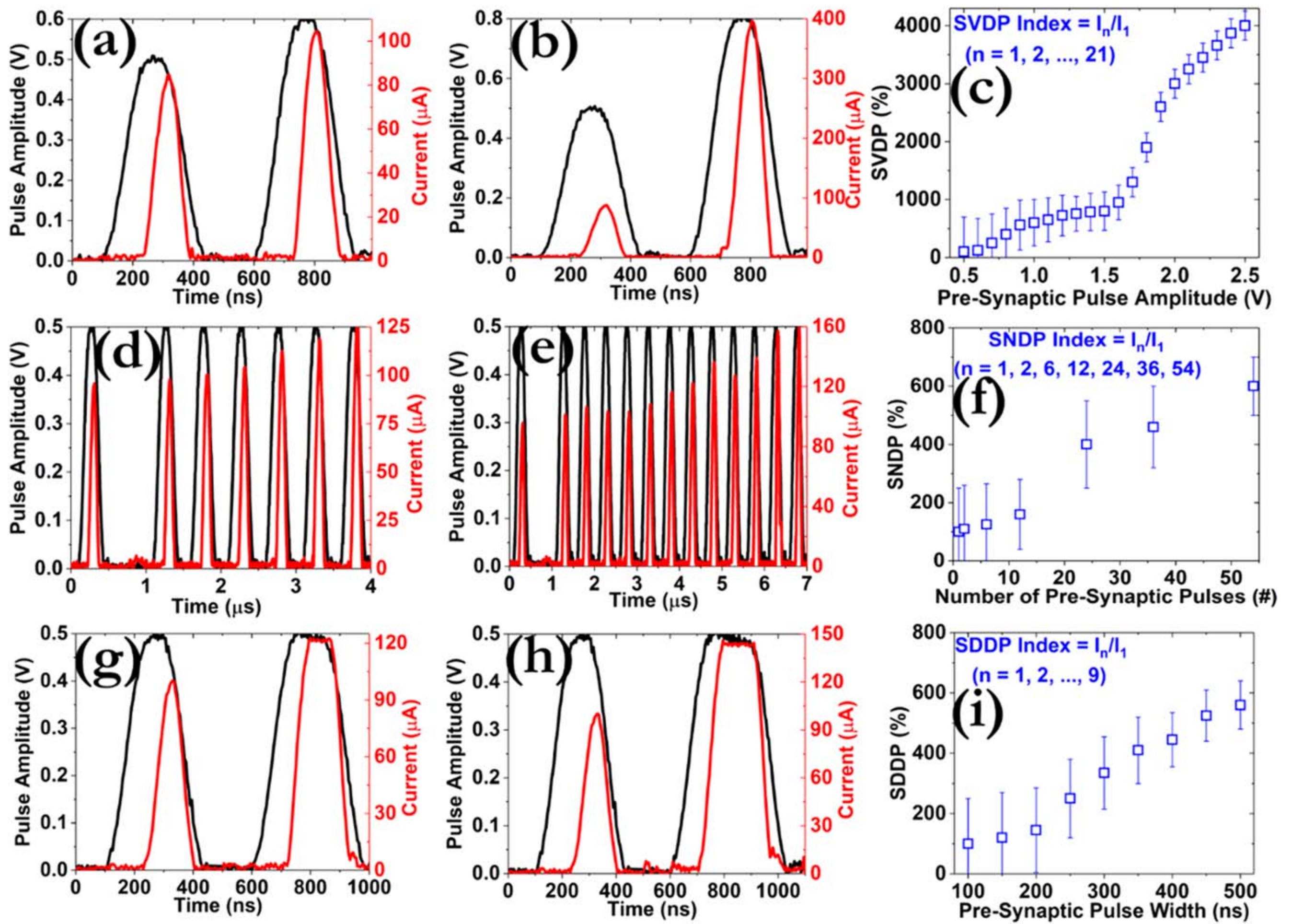

Fig. 18. (Color online) Experimental verification of the PPF effect as a function of the amplitude between the pre-synaptic pulses. 21 different pulse amplitudes were investigated by applying two successive pulses of 100 ns width and delay time while (a) and (b) disclose the post-synaptic responses for pulse amplitude of 0.6 V and 0.8 V, respectively. The amplitude of the first pre-synaptic pulse was always kept constant at 0.5 V, (c) distribution of the SVDP index (I_n/I_1) calculated by two consecutive pulses with amplitude $0.5 \leqslant V_p \leqslant 2.5V$ (I_1: 1st post-synaptic current, I_n: nth post-synaptic current, $n = 1, 2, 3, ..., 21$). Experimental verification of the PPF effect as a function of the number of pre-synaptic pulses. 7 different pulse sequences were explored by applying pulses of 0.5 V amplitude, 100 ns width and delay time while (d) and (e) divulges the post-synaptic responses by applying a total number of pulse train of 6 and 12, respectively. The train of the pulses was applied after the enforcement of a single pulse of 0.5 V amplitude and 100 ns width, whereas the delay time was set to 1 μs, (f) distribution of the SNDP index (I_n/I_1) estimated by the number of spikes ($n = 1, 2, 6, 12, 24, 36, 54$). Experimental verification of the PPF effect as a function of the width of two consecutive pre-synaptic pulses. 9 different pulse durations were studied by applying pulses of 0.5 V amplitude and 100 ns delay time, while (d) and (e) illustrate the post-synaptic responses for a pulse width of 150 ns and 200 ns, respectively. The width of the first pulse was always kept constant at $100ns$, (f) Distribution of the SDDP index (I_n/I_1) calculated by the number of spikes ($n = 1, 2, 3, ..., 9$).[69]

formation of a small CF, in terms of diameter, which becomes thinner when the applied pre-synaptic pulses are delivered with a smaller frequency. The only relation between the graphs depicted in Figs. 16(a) and 16(b) is the frequency modulation process. Moreover, under the application of high frequency (1 MHz) and regardless of the amplitude of the applied signal, a PPF is recorded.

Except for the above-mentioned synaptic plasticity properties, with the proposed device configuration we were able to imitate four different types of spike-dependent plasticity, namely SRDP, spike-voltage dependent plasticity (SVDP), spike-number dependent plasticity (SNDP) and spike-duration dependent plasticity (SDDP). All these neuromorphic functionalities were recorded by applying a train of square pulses with increasing amplitude (from 0.5 to 2.5 V), with a different number of pre-synaptic pulses (from 1 to 54) and with increasing width (from 100 to 500 ns). The acquired outcomes are presented in Figs. 17 and 18, whereas the fitting result that is presented in Fig. 17(c) was carried out by considering a Hebbian type STDP effect.[71,72] For the STDP effect, the values of 90 and 110 ns were estimated for the time scales of the respective effect, which are closely associated with the stability of the formed CF. This result is of great significance since denotes that the key factor that affects the dynamics of the whole memristive effect and permits the realization of bio-synaptic properties is the effective size of the percolated CF. Consequently, finding various ways, from a material point of view for tuning the properties of the CF lies behind the implementation of various neuromorphic functionalities. All these properties are quite important for the development of another type of ANNs, which are called spiking neural networks that exhibit enhanced properties in terms of low power consumption and elevated capabilities in processing real-time events.[73–76]

From the above-mentioned results, it can be argued that in the light of a crossbar configuration, the bipolar synaptic elements will be used as active elements for the synaptic weight update process, whereas the threshold switching cells

© 2022 The Author(s). Published on behalf of The Japan Society of Applied Physics by IOP Publishing Ltd

will be employed within a simple RC circuit to produce spikes.[77,78] From a material point of view, currently the CBRAM-based memory devices exhibit great advantages in contrast with their VCM counterparts, due to their low power consumption and their ability to operate under a dual switching mode (i.e. threshold and bipolar). For the implementation of artificial spiking activity, the Pt NPs-based samples seem quite promising due to the quite steep switching transitions, whereas the linear synaptic weight update property of the VO_x-based CBRAM is also attractive for reproducing artificial synaptic functionalities. The main focus of this work is the reproduction of synaptic behaviors, while neuron emulation will be the object of future research studies.

7. Conclusion

A thorough analysis was presented towards emulating a wide range of synaptic properties from a material point of view. VCM and CBRAM device configurations were examined to investigate their capability to emulate various neuromorphic properties. More specifically, the influence of the metal oxide stack, including the incorporation of one-layer, bilayer, or trilayer structures, as well as the integration of Pt NPs as bottom inactive electrode or as an intermediate layer with the memory stack were thoroughly examined. The common denominator of these approaches is to tune the properties of the CF for acquiring the desired synaptic pattern. In addition, the low power consumption of the proposed devices in combination with their inherent stochasticity characteristics offer unique advantages in mimicking the respective biological procedures of the human brain. It is thus apparent that the selected material structure direct impacts the ability of the memristive devices to operate as functional building blocks of an ANN as robust synaptic elements.

Acknowledgments

The authors would like to acknowledge the support of this work by the Hellenic Foundation for Research and Innovation (H.F.R.I.) under the "First Call for H.F.R.I. Research Projects to support Faculty members and Researchers and the procurement of high-cost research equipment grant" (Project No.: 3830).

ORCID iDs

Panagiotis Bousoulas https://orcid.org/0000-0002-5395-0777

Stavros Kitsios https://orcid.org/0000-0001-5046-1428
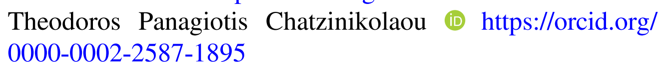
Theodoros Panagiotis Chatzinikolaou https://orcid.org/0000-0002-2587-1895

Iosif-Angelos Fyrigos https://orcid.org/0000-0001-8032-1725

Vasileios Ntinas https://orcid.org/0000-0002-2367-5567
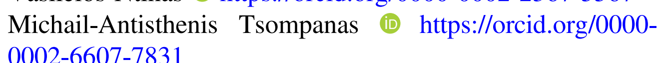
Michail-Antisthenis Tsompanas https://orcid.org/0000-0002-6607-7831

Georgios Ch. Sirakoulis https://orcid.org/0000-0001-8240-484X

Dimitris Tsoukalas https://orcid.org/0000-0001-5189-3396

1) L. Chua, G. C. Sirakoulis, and A. Adamatzky A (ed.) *Handbook of Memristor Networks* (Springer, Berlin, 2019).
2) D. B. Strukov, Nature **476**, 403 (2011).
3) D. Silver et al., Nature **529**, 484 (2016).
4) I. Vourkas and G. Ch, *Sirakoulis, Memristor-Based Nanoelectronic Computing Circuits and Architectures* (Springer, Berlin, 2015).
5) I. Vourkas and G. C. Sirakoulis, IEEE Circuits Syst. Mag. **16**, 15 (2016).
6) S. K. Esser et al., Proc. Natl Acad. Sci. **41**, 113 (2016).
7) G. Indiveri et al., Front. Neurosci. **5**, 73 (2011).
8) V. Ntinas, I. Vourkas, G. C. Sirakoulis, and A. Adamatzky, IEEE Trans. Circuits Syst : I. Regular Papers **64**, 1552 (2017).
9) V. Ntinas, I. Vourkas, A. Abusleme, G. Ch, Sirakoulis, and A. Rubio, IEEE Trans. Neural Networks Learning Syst. **29**, 5098 (2018).
10) T. P. Chatzinikolaou, I.-A. Fyrigos, V. Ntinas, S. Kitsios, P. Bousoulas, M.-A. Tsompanas, D. Tsoukalas, and G. C. Sirakoulis, 10th Int. Conf. on Modern Circuits and Systems Technologies (MOCAST), 2021.
11) T. P. Chatzinikolaou, I.-A. Fyrigos, V. Ntinas, S. Kitsios, P. Bousoulas, M.-A. Tsompanas, D. Tsoukalas, and G. C. Sirakoulis, 17th Int. Workshop on Cellular Nanoscale Networks and their Applications (CNNA), 2021.
12) T. P. Chatzinikolaou, I.-A. Fyrigos, V. Ntinas, S. Kitsios, P. Bousoulas, M.-A. Tsompanas, D. Tsoukalas, A. Adamatzky, and G. C. Sirakoulis, 28th IEEE Int. Conf. on Electronics, Circuits, and Systems (ICECS), 2021.
13) G. Papandroulidakis, I. Vourkas, A. Abusleme, G. Ch, Sirakoulis, and A. Rubio, IEEE Trans. Nanotechnol. **16**, 491 (2017).
14) C.-Y. Wang, C. Wang, F. Meng, P. Wang, S. Wang, S.-J. Liang, and F. Miao, Adv. Electron. Mater. **6**, 1901107 (2019).
15) C. Mahata, M. Ismail, and S. Kim, Appl. Phys. Lett. **119**, 221601 (2021).
16) C. Li et al., Nat. Electron. **1**, 52 (2018).
17) B. C. Jang, S. Kim, S. Y. Yang, J. Park, J.-H. Cha, J. Oh, J. Choi, S. G. Im, V. P. Dravid, and S.-Y. Choi, Nano Lett. **19**, 839 (2019).
18) T. Tuma, A. Pantazi, M. L. Gallo, A. Sebastian, and E. Eleftheriou, Nat. Nanotechnol. **11**, 693 (2016).
19) G. C. Adam, A. Khiat, and T. Prodromakis, Nat Commun. **9**, 5267 (2018).
20) A. F. Vincent, J. Larroque, N. Locatelli, N. Ben Romdhane, O. Bichler, C. Gamrat, W. S. Zhao, J.-O. Klein, S. G. -Retailleau, and D. Querlioz, IEEE Trans. Biomed. Circuits Syst. **9**, 166 (2015).
21) Z. Wang et al., Nat. Electron. **1**, 137 (2018).
22) V. Mnih et al., Nature **518**, 529 (2015).
23) J. J. Harris, R. Jolivet, and D. Attwell, Neuron **75**, 762 (2012).
24) S. Pi, C. Li, H. Jiang, W. Xia, H. Xin, J. J. Yang, and Q. Xia, Nat. Nanotechnol. **14**, 35 (2019).
25) S. Menzel, U. Böttger, M. Wimmer, and M. Salinga, Adv. Funct. Mater. **25**, 6306 (2015).
26) W. Banerjee, S. H. Kim, S. Lee, D. Lee, and H. Hwang, Adv. Electron. Mater **7**, 2100022 (2021).
27) K. Zarudnyi, A. Mehonic, L. Montesi, M. Buckwell, S. Hudziak, and A. J. Kenyon, Front. Neurosci **12**, 57 (2018).
28) V. Ntinas, A. Rubio, and G. Ch Sirakoulis, IEEE Access **9**, 983 (2020).
29) V. Ntinas, A. Rubio, G. C. Sirakoulis, E. S. Aguilera, M. Pedro, A. Crespo-Yepes, J. Martin-Martinez, R. Rodriguez, and M. Nafria, IEEE Trans. Circuits Syst. :II. Express Briefs **68**, 1378 (2020).
30) L. Bao et al., ACS Appl. Mater. Interfaces **11**, 44 (2019).
31) X. Ji, C. Wang, K. G. Lim, C. C. Tan, T. C. Chong, and R. Zhao, ACS Appl. Mater. Interfaces **11**, 23 (2019).
32) T. Takeuchi, A. J. Duszkiewicz, and R. G. M. Morris, Philos. Trans. R. Soc. B **369**, 20130288 (2014).
33) A. E. Pereda, Nat. Rev. Neurosci. **15**, 250 (2014).
34) J. G. Nicholls, A. R. Martin, P. A. Fuchs, D. A. Brown, M. E. Diamond, and D. A. Weisblat, *From Neuron to Brain* (Sinauer Associates, Sunderland, MA, 2012).
35) D. A. Sousa, *How the Brain Learns* (Corwin Press, Oaks, CA, 2006).
36) W. C. Abraham, Nat. Rev. Neurosci. **9**, 387 (2008).
37) M. Chistiakova, N. M. Bannon, M. Bazhenov, and M. Volgushev, Neuroscientist **20**, 483 (2014).
38) J. Wang and F. Zhuge, Adv. Mater. Technol. **4**, 1800544 (2019).
39) F. Cai, J. M. Correll, S. H. Lee, Y. Lim, V. Bothra, Z. Zhang, M. P. Flynn, and W. D. Lu, Nat. Electron. **2**, 290 (2019).
40) Y. Xi, B. Gao, J. Tang, A. Chen, M.-F. Chang, X. S. Hu, J. van der Spiegel, H. Qian, and H. Wu, Proc. IEEE. **109**, 14 (2021).
41) P. Bousoulas, P. Asenov, I. Karageorgiou, D. Sakellaropoulos, S. Stathopoulos, and D. Tsoukalas, J. Appl. Phys. **120**, 154501 (2016).
42) P. Bousoulas, I. Michelakaki, and D. Tsoukalas, J. Appl. Phys. **115**, 034516 (2014).
43) P. Bousoulas, I. Karageorgiou, V. Aslanidis, K. Giannakopoulos, and D. Tsoukalas, Phys. Status Solidi A **215**, 1700440 (2017).
44) P. Bousoulas, S. Stathopoulos, D. Tsialoukis, and D. Tsoukalas, IEEE Electron Devices Lett. **37**, 874 (2016).
45) M. Tsigkourakos, P. Bousoulas, V. Aslanidis, E. Skotadis, and D. Tsoukalas, Phys. Status Solidi A **214**, 1700570 (2017).

© 2022 The Author(s). Published on behalf of The Japan Society of Applied Physics by IOP Publishing Ltd

46) P. Bousoulas, I. Giannopoulos, P. Asenov, I. Karageorgiou, and D. Tsoukalas, J. Appl. Phys. **121**, 094501 (2017).
47) P. Bousoulas, I. Michelakaki, and D. Tsoukalas, Thin Solid Films **571**, 23 (2014).
48) P. Bousoulas and D. Tsoukalas, *Advanced Engineering Materials and Modeling* (Wiley, New York, 2016) Vol. 369.
49) P. Bousoulas, I. Michelakaki, J. Giannopoulos, K. Giannakopoulos, and D. Tsoukalas, MRS Online Proc. Library **1729**, 1 (2014).
50) M. Uenuma, B. Zheng, K. Kawano, M. Horita, Y. Ishikawa, I. Yamashita, and Y. Uraoka, Appl. Phys. Lett. **100**, 083105 (2012).
51) P. Bousoulas, J. Giannopoulos, K. Giannakopoulos, P. Dimitrakis, and D. Tsoukalas, Appl. Surf. Sci. **332**, 55 (2015).
52) K. Giannakopoulos, J. Giannopoulos, P. Bousoulas, E. Verrelli, and D. Tsoukalas, 2nd Int. Multidisciplinary Microscopy and Microanalysis Congress, 2015 **Vol. 9**.
53) D. Sakellaropoulos, P. Bousoulas, and D. Tsoukalas, J. Appl. Phys. **126**, 044501 (2019).
54) P. Bousoulas, D. Sakellaropoulos, J. Giannopoulos, and D. Tsoukalas, Proc. 45th European Solid State Device Research Conf. (ESSDERC) (IEEE), 2015, p. 274.
55) Q. Wu, W. Banerjee, J. Cao, Z. Ji, L. Li, and M. Liu, Appl. Phys. Lett. **113**, 023105 (2018).
56) P. Bousoulas, I. Michelakaki, E. Skotadis, M. Tsigkourakos, and D. Tsoukalas, IEEE Trans. Electron Devices **64**, 2468 (2017).
57) D. Sakellaropoulos, P. Bousoulas, G. Nikas, C. Arvanitis, E. Bagakis, and D. Tsoukalas, Microelectron. Eng. **229**, 111358 (2020).
58) N. Shukla, R. K. Ghosh, B. Grisafe, and S. Datta, 2017 Int. Electron Devices Meeting (IEDM), 2017 (IEEE, San Francisco, CA), p. 17.
59) W. Wang, M. Wang, E. Ambrosi, A. Bricalli, M. Laudato, Z. Sun, X. Chen, and D. Ielmini, Nat. Commun. **10**, 81 (2019).
60) P. Bousoulas, D. Sakellaropoulos, C. Papakonstantinopoulos, S. Kitsios, C. Arvanitis, E. Bagakis, and D. Tsoukalas, Nanotechnology **31**, 454002 (2020).
61) J. D. McBrayer, R. M. Swanson, T. W. Sigmion, and J. Bravman, J. Appl. Phys. Lett. **43**, 653 (1983).
62) P. Bousoulas, M. Panagopoulou, N. Boukos, and D. Tsoukalas, J. Phys. D: Appl. Phys. **54**, 225303 (2021).
63) D. Sakellaropoulos, P. Bousoulas, C. Papakonstantinopoulos, S. Kitsios, and D. Tsoukalas, IEEE Trans. Electron Devices **68**, 1598 (2021).
64) D. Sakellaropoulos, P. Bousoulas, C. Papakonstantinopoulos, S. Kitsios, and D. Tsoukalas, IEEE Electron Devices Lett **41**, 1013 (2020).
65) P. Bousoulas, D. Sakellaropoulos, and D. Tsoukalas, Appl. Phys. Lett. **118**, 143502 (2021).
66) F. Lacy, IEEE Sens. J. **9**, 1111 (2009).
67) C. Papakonstantinopoulos, P. Bousoulas, M. Tsigkourakos, D. Sakellaropoulos, L. Sygellou, and D. Tsoukalas, ACS Appl. Electron. Mater. **3**, 2729 (2021).
68) J.-P. Monchoux, M. Dollé, P. Rozier, and J. Galy, Solid State Ionics **182**, 24 (2011).
69) P. Bousoulas, C. Papakonstantinopoulos, S. Kitsios, K. Moustakas, G. Ch Sirakoulis, and D. Tsoukalas, Micromachines **12**, 306 (2021).
70) R. M. Shiffrin and R. C. Atkinson, Psychol. Rev. **76**, 179 (1969).
71) R. S. Zucker and W. G. Regehr, Annu. Rev. Physiol. **64**, 355 (2002).
72) W. Xu et al., Nano Energy **48**, 575 (2018).
73) Y. Zhang et al., Appl. Phys. Rev. **7**, 011308 (2020).
74) A. Ascoli, S. Slesazeck, H. Mähne, R. Tetzlaff, and T. Mikolajick, IEEE Trans. Circuits Syst.: I. Reg. Papers **62**, 1165 (2015).
75) A. Ascoli, A. S. Demirkol, R. Tetzlaff, S. Slesazeck, T. Mikolajick, and L. O. Chua, Front. Neurosci. **15**, 651452 (2021).
76) A. Ascoli, A. S. Demirkol, R. Tetzlaff, and L. O. Chua, IEEE Trans. Circuits Syst. I: Regular Papers **69**, 3 (2022).
77) P. Bousoulas, C. Tsioustas, J. Hadfield, V. Aslanidis, S. Limberopoulos, and D. Tsoukalas, IEEE Trans. Electron Devices **69**, 2360 (2022).
78) P. Bousoulas, C. Tsioustas, J. Hadfield, V. Aslanidis, S. Limberopoulos, and D. Tsoukalas, IEEE Trans. Electron Devices **69**, 2368 (2022).

© 2022 The Author(s). Published on behalf of The Japan Society of Applied Physics by IOP Publishing Ltd